Available online at www.sciencedirect.com

jmr&t Journal of Materials Research and Technology

journal homepage: www.elsevier.com/locate/jmrt

Thermoelectric behavior of $Bi_2Te_{2.55}Se_{0.45}$ with a tunable seebeck coefficient: A comparison between coarse needle-like structure and bulk nanostructured alloys

Farah M. El-Makaty [a], *R.A. Shakoor* [a,b], *Abdelmagid Hammuda* [a], *Khaled M. Youssef* [c,*]

[a] *Mechanical and Industrial Engineering Department, Qatar University, Doha 2713, Qatar*
[b] *Center of Advanced Materials, Qatar University, Doha 2713, Qatar*
[c] *Materials Science and Technology Graduate Program, College of Arts and Sciences, Qatar University, Doha 2713, Qatar*

ARTICLE INFO

Article history:
Received 22 August 2023
Accepted 9 October 2023
Available online 12 October 2023

Keywords:
Thermoelectric
Seebeck coefficient
Mechanical milling
Induction melting
Bismuth telluride

ABSTRACT

In this study, we compare the thermoelectric properties of coarse-grained n-type $Bi_2Te_{2.55}Se_{0.45}$ alloy prepared by induction melting with the bulk-nanostructured prepared by ball milling and hot-pressing techniques. The corresponding thermoelectric properties showed different behavior for each material processed using different routes. The most striking result of the study is observing a p-type behavior and charge carrier transition from p-to n-type for the coarse-grained alloy. These observed phenomena are related mainly to the unique needle-like microstructure accompanied by high lattice strain. Lastly, the obtained figure-of-merit values for the coarse needle-like structure and bulk nanostructured $Bi_2Te_{2.55}Se_{0.45}$ alloys are 0.20 and 0.80 at their optimum temperatures of 60 and 120 °C, respectively.

1. Introduction

The demand for clean energy is rising due to the increased greenhouse emissions leading to global warming. In this regard, thermoelectric devices offer an eco-friendly source of electricity that is reliable, noise-free, and does not require any moving parts [1]. Many thermoelectric materials are being explored for power generation applications, such as GeTe [2–4], and PbTe [5–8], half-Heusler compounds [9–13], BiS [14], CuSe [15,16], InSb [17,18], Cu_3N [19], and SnSe [20,21]. One advantage of binary and ternary semiconductors is the ability to control their physical properties in different methods, for example, by changing the production route or tuning intrinsic composition [22]. Most thrillingly, in a few instances, it is possible to change the charge carrier type, causing a shift from p-to n-type conduction or vice versa. This possibility of attaining both n-type and p-type semi-conductivity in a single material system is an attractive feature for thermoelectric application in power generation as it gives wider options for synthesis.

* Corresponding author. Materials Science and Technology Graduate Program, College of Arts and Sciences, Qatar University, Doha 2713, Qatar.
E-mail address: Kyoussef@qu.edu.qa (K.M. Youssef).
https://doi.org/10.1016/j.jmrt.2023.10.087

Bismuth telluride (Bi_2Te_3) represents the benchmark of thermoelectric materials used for near-room temperature applications [23–26]. The efficiency of a thermoelectric material can be assessed using the figure-of-merit (ZT) value defined as

$$ZT = \frac{S^2\sigma}{k} T \quad (1)$$

where S is the Seebeck coefficient, σ is the electrical conductivity, T is the absolute temperature, and κ is the total thermal conductivity. To improve the performance of a thermoelectric material, it is desired to either boost the power factor (PF, the product of $S^2\sigma$) and/or lower the overall thermal conductivity. However, these parameters are interdependent, making it difficult to fully control the final thermoelectric properties.

Moreover, the effectiveness of a thermoelectric device depends equally on its two junctions, the n- (negative charge carriers' part) and p- (positive charge carriers' part) types at a given operating temperature. Even though the p-type, bismuth antimony telluride $(Bi,Sb)_2Te_3$, is reported to have high ZT values of around 1.5, its countertype, bismuth tellurium selenide, $Bi_2(Te,Se)_3$ has much lower ZT around 1 [27–29]. This inefficiency of the n-type has limited the current applications of these alloys to low-power generators only. The main reason for low ZT in n-type $Bi_2(Te,Se)_3$ is the strong anisotropy [30]. Bi_2Te_3 is composed of Bi and Te layers ordered as Te(1)-Bi-Te(2)-Bi-Te(1) [31,32]. Selective preference of Te(2) sites during Se doping causes directional preference in the carrier transport properties (σ and κ), which are reported to be superior along a-b planes [30,33].

One way to achieve higher thermoelectric properties in $Bi_2(Te,Se)_3$ alloys is through texturing and utilizing the higher in-plane properties. Zone melting is a popular commercial technique that is used to fabricate highly oriented polycrystalline Bi_2Te_3 ingots [34,35]. The drawback of this technique is that it produces poor mechanical properties. Thus, the ongoing research to enhance the ZT of n-type $Bi_2(Te,Se)_3$ alloys mainly focuses on nanostructuring through powder metallurgy as it is effective in enhancing the thermoelectric properties and producing reliable thermoelectric devices with improved mechanical properties [33]. The nanostructuring method results in highly dense grain boundaries that effectively reduce the thermal conductivity parameter [36–40]. Studies revealed that selective scattering of phonons could lower the lattice thermal conductivity while maintaining high values of the remaining thermoelectric properties, thus improving the ZT value [41,42]. Numerous studies have reported the thermoelectric performance of nanostructured $Bi_2(Te,Se)_3$ alloys [36,43]; however, only limited improvements are achieved as some underlying mechanisms of charge carrier transitions and defects are yet to be further studied and explored. In fact, mechanical deformation through powder metallurgy can intensively produce point defects, which in return induces a donor-like effect and an increase in carrier concentration (n_c) [35]. However, instability in n_c and reduced carrier mobility (μ) usually offsets the gain from decreasing the thermal conductivity [30,35,42,44]. Moreover, the defect chemistry in $Bi_2(Te,Se)_3$ alloys is complicated as both electron- and hole-producing defects are present and own comparable formation energies, leading to either strong n-type or severely compensated alloys [45].

In this study, we investigated the thermoelectric properties of coarse-grained and bulk nanostructured $Bi_2Te_{2.55}Se_{0.45}$ alloys. The same alloy composition is prepared via two different processes: induction melting (coarse-grained route) and mechanical alloying followed by hot pressing (bulk nanostructured route). The thermoelectric behavior and defect chemistry as a function of the produced structure are studied, and a charge carrier transition from p-to n-type is reported in $Bi_2Te_{2.55}Se_{0.45}$ alloy.

2. Methodology

2.1. Materials and synthesis of coarse-grained $Bi_2Te_{2.55}Se_{0.45}$

Pure elemental shots of bismuth (5 N), tellurium (2–5 mm, 5 N), and selenium (5 N) from ESPI metals were used to prepare $Bi_2Te_{2.55}Se_{0.45}$ alloy. The weighted elements were loaded into an 18 mm-diameter tungsten carbide die and sealed inside the quartz tube of a copper-boat induction furnace (Edmund Buhler GmbH, Germany). The quartz tube was evacuated and refilled several times with ultrahigh-pure (UHP) argon. An induction coil was slid around the quartz tube, and the elements were melted using a radio frequency (RF) induction generator with a working frequency of 200 kHz and a power of 12 kW. Before melting the Bi, Te, and Se components, a Ti getter was melted to absorb any residual oxygen contents in the tube's atmosphere. The process was repeated two times to ensure complete mixing.

After the induction melting process, the surface of the solidified 18 mm-diameter BiTeSe disc was rough. Thus, the solidified discs were hot pressed (HP) using an 18 mm tungsten carbide die at 350 °C, 0.8 GPa, and a holding time of 10 min. The HP process was carried out under a UHP argon atmosphere. Finally, a homogenization process of the hot-pressed discs was carried out using a tube furnace (GSL-1500X-RTP50). The homogenization procedure was performed at 300 °C for 6 h under mixed gas (2 % hydrogen, 98 % argon) (Fig. 1a).

2.2. Materials and synthesis of nanostructured $Bi_2Te_{2.55}Se_{0.45}$

Elemental powders of bismuth (−100 mesh, 99.99 %, Sigma-Aldrich), tellurium (−30 mesh, 99.997 %, Sigma-Aldrich), and selenium (−325, 99.5 %, Alfa Aesar) were used to prepare the $Bi_2Te_{2.55}Se_{0.45}$ alloy. The powders were milled in a stainless-steel vial under a UHP argon atmosphere (O_2 < 0.5 ppm) via a SPEX milling device (SamplePrep, 8000 M) for 20 h with a ball-to-powder ratio of 7:1. The milled powders were then hot pressed under a UHP argon atmosphere using an 18 mm tungsten carbide die at 300 °C and 0.5 GPa for 5 min (Fig. 1b). The applied parameters of temperature and pressure are based on previously optimized hot press conditions [41].

2.3. Characterization

Phase identification of the coarse-grained and the nanostructured $Bi_2Te_{2.55}Se_{0.45}$ samples was investigated by X-ray

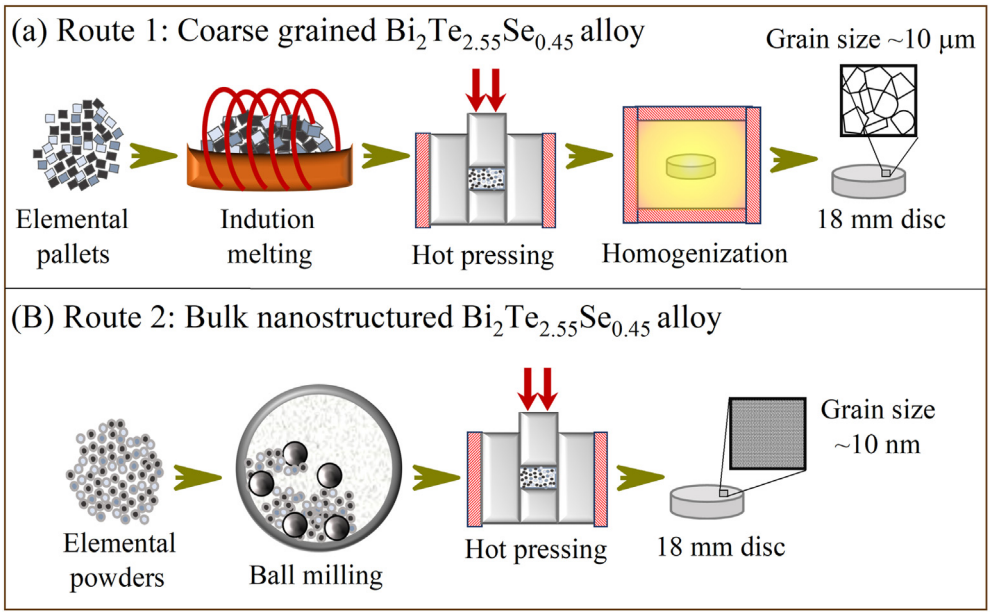

Fig. 1 – Experimental work schematic for the two different routes employed. (a) Induction melting/hot pressing/homogenization and (b) ball milling/hot pressing techniques.

diffraction (XRD: PANalytical, EMPYREAN) using a radiation source of Cu/Kα (λ = 1.54 Å). The morphology and elemental mapping of the final discs were analyzed using scanning electron microscopy (SEM) (Nano-SEM Nova 450, FEI-USA) equipped with energy-dispersive X-ray spectroscopy (EDS). After milling, the structural features and the grain size of the nanopowder sample were investigated using a transmission electron microscope (TEM) (Tecnai G2 FEG 200 kV, FEI). The TEM sample was prepared by sonicating the powder in isopropyl alcohol using an Ultra-sonicator bath for 20 min. The sonicated material was drop-casted onto a 300-mesh carbon-film-covered copper gird. TEM analysis was also performed for the ball-milled/hot-pressed disc. The TEM sample preparation was performed using a focused ion beam (FEI Helios NanoLab™ G4 FIB/SEM) dual system, and then the nanostructure was examined by an FEI Titan™ 60–300 TEM. The microstructure of the sample prepared by induction melting was examined using optical microscopy. The disc was mirror-polished and etched using a 1:1 solution of HNO_3 and HCl for 10 s. The etched surface was then rinsed with acetic acid and cleaned with water. After etching, an optical microscope (BX53 M OLYMPUS, Japan) was used to obtain surface images. The density of the prepared discs was measured based on the Archimedes principle using the Sartorius density determination kit (Sartorius YDK03, Germany). The density determination kit was set up using distilled water, and the water's temperature was monitored during the measurements.

2.4. *Thermoelectric properties measurements*

The electrical conductivity and the Seebeck coefficient were measured simultaneously for a temperature range of 25–300 °C under a UHP argon atmosphere using the SBA 485 Nemesis – NETZSCH device. The thermal conductivity was measured using the C-therm trident device (MTPS Guard Ring Technology, Canada) with a thermal joint compound (type 120 silicone) as a contact agent. The measurements were performed in the temperature range of 25–150 °C. The measurements for each sample were repeated two times, and the data standard deviation was less than 5 %.

3. Results and discussion

Mechanical alloying and induction melting processes are broadly accepted methods for preparing metals and alloys in nano- and coarse-grained sizes, respectively. The phase formation of the $Bi_2Te_{2.55}Se_{0.45}$ alloys prepared using these two techniques was studied and analyzed by XRD, as shown in Fig. 2. Diffraction patterns of both samples can be indexed to the standard diffraction data of a single-phase rhombohedral $Bi_2Te_{2.55}Se_{0.45}$ inorganic alloy with a space group R-3m (card no. 98-024-7619) [46]. The rest of the peaks (marked with *) were matched with pure Te with a hexagonal crystal structure (space group P312).

Moreover, broader peaks are noticed for the induction melted sample. According to Debye-Scherrer and Warren-Averbach models [41,47], the width of XRD peaks is related to grain size and internal stresses within the sample, where small grains and high lattice strain broaden the peaks. Since the grain size is quite large (micrometer range) in the induction melting sample, the broadness of peaks is mainly caused by high internal strain (e.g., due to intrinsic defects).

In addition, the XRD results were quantified by calculating the texture coefficient $T_{c(hkl)}$ based on five peaks (015), (1010), (110), (0015), and (205). The $T_{c(hkl)}$ factor was calculated for each orientation using [48]:

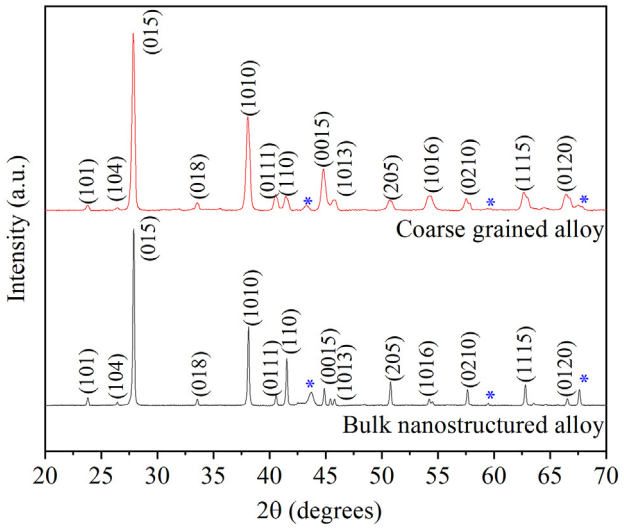

Fig. 2 – XRD patterns for the coarse-grained and bulk nanostructured $Bi_2Te_{2.55}Se_{0.45}$ discs.

$$T_{c(hkl)} = \frac{I_{(hkl)}/I_{0(hkl)}}{(1/N)\left[\sum_N I_{(hkl)}/I_{0(hkl)}\right]} \quad (2)$$

where $I_{(hkl)}$ is the measured intensity of the peak, $I_{0(hkl)}$ is the relative intensity corresponding to the plane of reference $Bi_2Te_{2.55}Se_{0.45}$, and N is the number of reflections. Interestingly, a high $T_{c(1010)}$ factor of 1.3 in coarse-grained alloy and 1.28 in the bulk nanostructured alloy is noticed. Also, $T_{c(0015)}$ had a factor of 2.49 in coarse-grained alloy and 1.25 in the bulk nanostructured alloy, implying preferred orientation in (1010) and (0015) planes in both samples.

It is known that the thermoelectric properties of materials produced by mechanical alloying are greatly influenced by the morphology and size of the milled powder [49]. Thus, SEM imaging was employed to study the milled n-type $Bi_2Te_{2.55}Se_{0.45}$ powder (after 20 h of milling), and the results are shown in Fig. 3. The SEM images reveal irregular shapes and rough surfaces of the milled powders, while the EDS elemental mapping shows a uniform distribution of elements throughout the sample.

More investigation on the $Bi_2Te_{2.55}Se_{0.45}$ powders was performed using TEM analysis, and the obtained results are shown in Fig. 4. Bright and dark-field TEM images in Figs. 4a and 5b reveal equiaxed and randomly distributed grains within the particle. The grain size distribution was calculated from several dark-field images, and the average grain size is found to be 13 ± 4 nm with no grains above 30 nm (Fig. 4c). The electron diffraction pattern shown in Fig. 4d reveals the atomic planes of the single-phase rhombohedral $Bi_2Te_{2.55}Se_{0.45}$ nanograins, matching well with the XRD patterns shown in Fig. 2. High-resolution TEM image in Fig. 4e reflects the interplanar distance (0.321 nm) for the main (015) peak in the $Bi_2Te_{2.55}Se_{0.45}$ sample. After consolidating the milled powders using hot pressing, it is expected that grain growth might take place due to the relatively high temperature during consolidation. Fig. 5 shows a bright-field TEM image for the consolidated $Bi_2Te_{2.55}Se_{0.45}$ disc along with the corresponding electron diffraction pattern (Fig. 5 inset). After hot pressing, the grain size increased to about 40–90 nm.

For the coarse-grained $Bi_2Te_{2.55}Se_{0.45}$ sample prepared by induction melting/hot pressing/homogenization processes, the microstructure was revealed by etching the surface with HCL and HNO_3, and the optical images are shown in Fig. 6. The microstructure, interestingly, shows a randomly distributed needle-like structure, of which the width ranges from 10 to 60 μm and the length about 300–900 μm, present throughout the entire surface of the disc. The shape and dimensions of the needle-like structure are suggested to significantly impact the thermoelectric properties of the sample, especially the electrical conductivity [50]. Zhu et al. [51] produced $Bi_2Te_{2.7}Se_{0.3}$ via melting in a ceramic crucible and observed unique elongated grains due to the nonequilibrium cooling during the solidification process. Their samples also revealed similar peak broadening in XRD, indicating that the internal lattice strain is mainly caused by the unique martensite-like microstructure. Hence, the observed high lattice strain in the XRD is suggested to be caused by the needle-like microstructure and its associated induced defects [34]. To better understand the distribution of elements within the structure, EDS elemental mapping was carried out on the etched disc. Fig. 7 shows a uniform distribution of all elements within the needle-like structure.

Thermoelectric properties were measured for the samples, and electrical conductivity results are shown in Fig. 8. As presented, the electrical conductivity for the needle-like microstructure sample increases with increasing temperature, indicating a typical semiconductor behavior. Meanwhile, the electrical conductivity for the bulk nanostructured sample decreases till it reaches a minimum at a temperature of 180 °C, then rises again as the temperature increases. This indicates that the behavior switches from a metallic phase to a semiconductor phase at the stated temperature. Nevertheless, the electrical conductivity for the bulk nanostructured sample is less dependent on temperature since the maximum difference observed is about 35 S/cm. On another note, a higher electrical conductivity of ~300 S/cm for the bulk

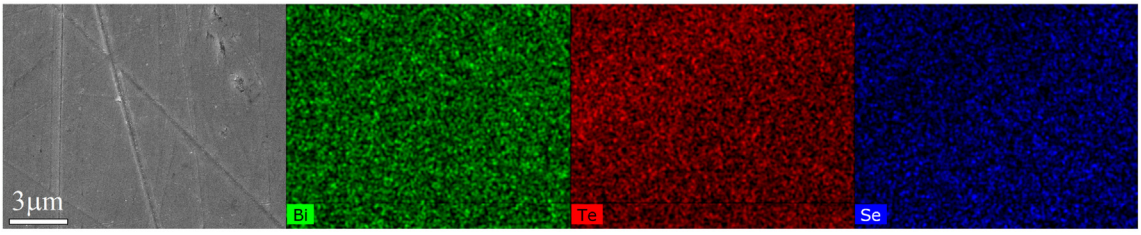

Fig. 3 – SEM imaging and elemental mapping for as milled $Bi_2Te_{2.55}Se_{0.45}$ powders.

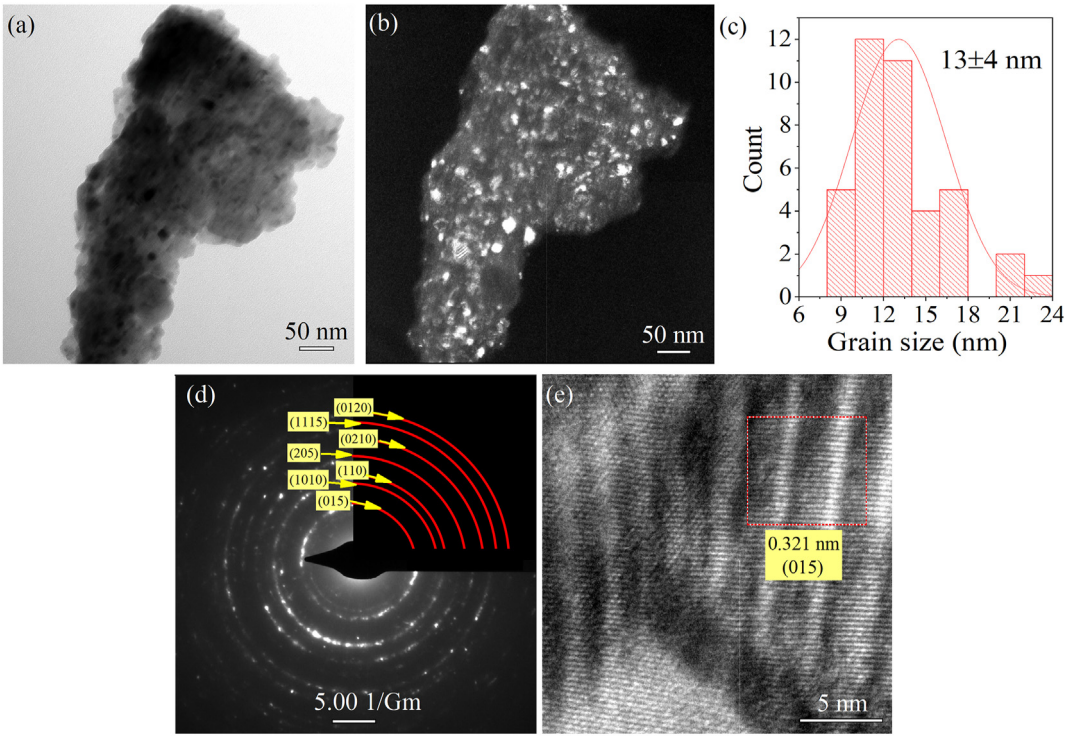

Fig. 4 – TEM analysis for milled $Bi_2Te_{2.55}Se_{0.45}$ powders (a) bright-field, (b) dark-field, (c) grain size distribution, (d) diffraction pattern, and (e) A high-resolution TEM image.

nanostructured $Bi_2Te_{2.55}Se_{0.45}$ sample is obtained compared with 100~220 S/cm for the needle-like microstructure alloy. The higher electrical conductivity values of the bulk nanostructured sample can be mainly attributed to the induced point defects through mechanical deformation. The most common defects in $Bi_2(Te,Se)_3$ alloys are Te, Bi, and Se vacancies (which provide two electrons, one hole, and 2 electrons per defect, respectively) resulting from the evaporation of consisting elements, as well as the anti-site defects of Bi atoms in Se and Te sites (providing one hole per defect) [44]. All these donor-like defects are intensively induced during the mechanical milling process, which greatly increases the charge carrier concentration, leading to high electrical conductivity. Meanwhile, the low electrical conductivity observed in the needle-like microstructure alloy can be attributed to the absence of alignment of the needle-like structure (as seen in the microstructure of this sample in Fig. 6), which significantly restricts the movement of charge carriers [52]. It is well-known that the layered structure of $Bi_2(Te,Se)_3$ alloys exhibits severe anisotropy that is sensitive to texture; hence the absence of alignment can cause carrier scattering, thereby degrading the carrier mobility [30].

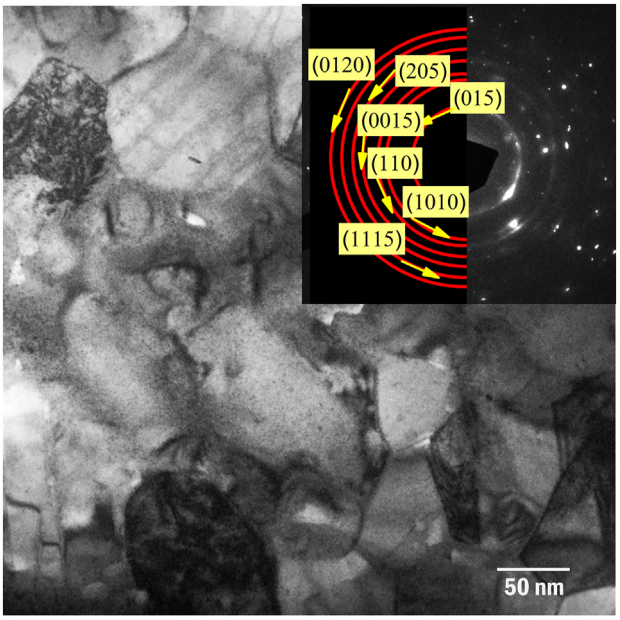

Fig. 5 – Bright-field TEM image for consolidated $Bi_2Te_{2.55}Se_{0.45}$ powders (inset: the corresponding diffraction pattern).

Seebeck coefficient values for both samples are presented in Fig. 8b. The bulk nanostructured $Bi_2Te_{2.55}Se_{0.45}$ sample showed an n-type behavior (negative Seebeck values), which is expected from Se-doped Bi_2Te_3 materials and is in agreement with the reported data [38,41,53]. The |S| value increases to $S_{max} = 203$ μV/K at 160 °C then decreases again due to the bipolar effect of minority charge carrier [41]. The strong n-type properties exhibited in this sample are most likely due to the donor-like effect introduced by the high-energy ball milling [35] and Se doping [49,54,55]. Another possible reason for the observed negative conduction is the volatilization of Se atoms during hot pressing, leading to electron generation [56,57]. This occurs because Se has a lower energy of evaporation (37.70 kJ/mol) compared to Bi (104.80 kJ/mol) [44], producing more V_{Se} vacancies in $Bi_2Te_{2.55}Se_{0.45}$ alloy [58–60].

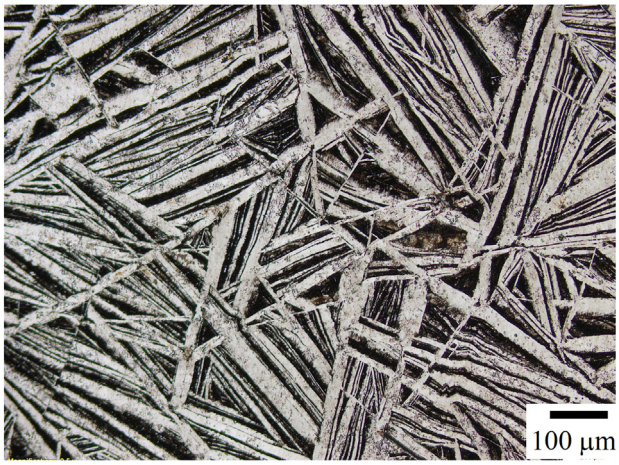

Fig. 6 – Microstructure images for induction melted $Bi_2Te_{2.55}Se_{0.45}$ disc.

On the other hand, the coarse-grained sample showed a p-type behavior and a transition from p-to n-type at high temperatures (T > 200 °C). The maximum Seebeck coefficient value is 197 μV/K, which occurs at a low temperature of 40 °C. This could indicate that the majority charge carriers at room temperature are p-type. It is also noticed that as the temperature increases, the n-type conduction rises. Adam et al. [61,62] prepared $Bi_2(Se_{1-x}Te_x)_3$ alloys with x = 0, 0.3, 0.6, 0.7 and 0.9 using conventional melting methods. The authors reported that partial substitution of Se by Te reduces the p-type charge conduction monotonically and raises the n-type charge conduction. In their study, the highest Seebeck values observed were 55 and 37 μV/K for x = 0 and 0.3, respectively, while a weak p-to n-type transition [from ~2 to −5 μV/K] occurred in the rest of samples.

The source of high hole concentration at room temperature in the coarse-grained sample mainly originates from internal structural defects, which also explains the broadening of XRD peaks in this sample, as seen in Fig. 2 [42]. According to Hong et al. [63], anti-site defects are dominant in coarse-grained Bi_2Te_3, resulting in intrinsic p-type material. Moreover, Zhang et al. [33] explained that the formation energy of anti-site defects (of Bi in Te and Se sites) increases with Se alloying in $Bi_2(Te_{1-x}Se_x)_3$ alloys, and the p-n type transition occurs at the composition having the largest band gap $Bi_2Te_2Se_1$ (at x = 0.33). Hence, the low Se doping used in this study (x = 0.15) and the high density of anti-site defects caused by the microstructure of the sample could plausibly explain the p-type behavior at room temperature. The Seebeck results are significant because they show that it is possible to synthesize both p-type and n-type materials from the same elemental precursors (Bi, Te, and Se) by simply controlling the processing route chosen.

In order to get more insight into the factors affecting the thermoelectric parameters, the Goldsmid-Sharp relation was used to estimate the band gap (E_g) of the materials according to:

$$E_g = 2e|S_{max}|T_{max} \quad (3)$$

where S_{max} and T_{max} are the maximum Seebeck coefficient and the corresponding temperature, respectively [33]. The obtained E_g values are 0.12 and 0.17 eV for the coarse-grained and bulk nanostructured samples, respectively. Based on previous studies, a suitable band gap for efficient thermoelectric alloys is around 0.15–0.26 eV [64–67]. However, there is no doubt that there is an optimum band gap for each thermoelectric material. Greenaway et al. [68] reported that increasing x in $Bi_2(Te_{1-x}Se_x)_3$ alloys enlarges the band gap from ~0.14 to 0.30 eV ($E_{g\ max}$ at x = 0.33), then reduces it to ~0.16 eV. Consequently, the obtained E_g in this study for the coarse-grained sample is much less than the reported data for the alloy, which makes the intrinsic excitation occur easily and more sensitive to temperature [35]. This could explain the quick transition of the Seebeck coefficient from 194 μV/K at RT to −22 μV/K at 300 °C in this sample.

The measured total thermal conductivity is shown in Fig. 10a. Electronic ($\kappa_{electronic}$), bipolar ($\kappa_{bipolar}$), and lattice ($\kappa_{lattice}$) thermal conductivity were calculated and are shown in Fig. 10b–c. Here, Wiedemann–Franz law ($\kappa_e = \sigma LT$) was used to calculate $\kappa_{electronic}$ where σ is the electrical conductivity, L is Lorenz number of $L = 2 \times 10^{-8}\ V^2K^{-2}$, and T is the measured temperature [49,69]. Whereas the summation of $\kappa_{bipolar}$ and $\kappa_{lattice}$ was found by subtracting the total thermal conductivity from $\kappa_{electronic}$ ($\kappa_{total} = \kappa_{electronic} + \kappa_{bipolar} + \kappa_{lattice}$). As seen in Fig. 9a, the bulk nanostructured sample shows lower thermal conductivity (0.58 W/mK at RT) compared to the coarse-grained sample (0.75 W/mK at RT). The values of the bulk nanostructured sample match well with the reported data [70]. From Fig. 10b–c, it can be concluded that the reasons behind the lower thermal conductivity in the bulk nanostructured alloy could be attributed to lattice and bipolar factors. This is expected due to (i) lower particle adhesion caused by the ball milling/hot pressing technique compared to induction melting, (ii) suitable band gap which lowers the bipolar effect, as well as (iii) the high grain boundary density formed during milling, contributing to the increase in phonon scattering and lowering $\kappa_{Lattice}$. Meanwhile, even though $\kappa_{electronic}$ is very low in the coarse-grained sample, large $\kappa_{Lattice}$

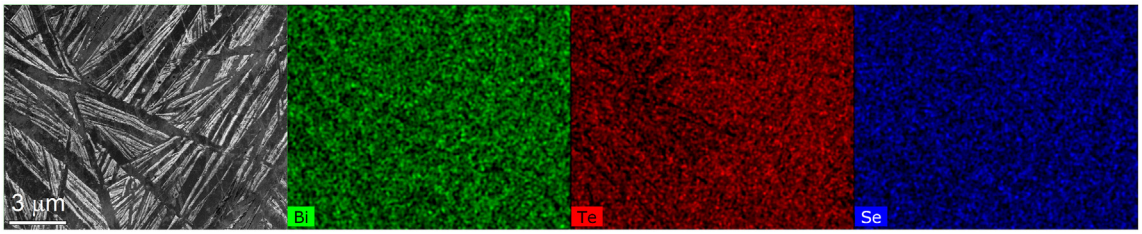

Fig. 7 – SEM image and the EDS mapping of the etched induction melted $Bi_2Te_{2.55}Se_{0.45}$ disc.

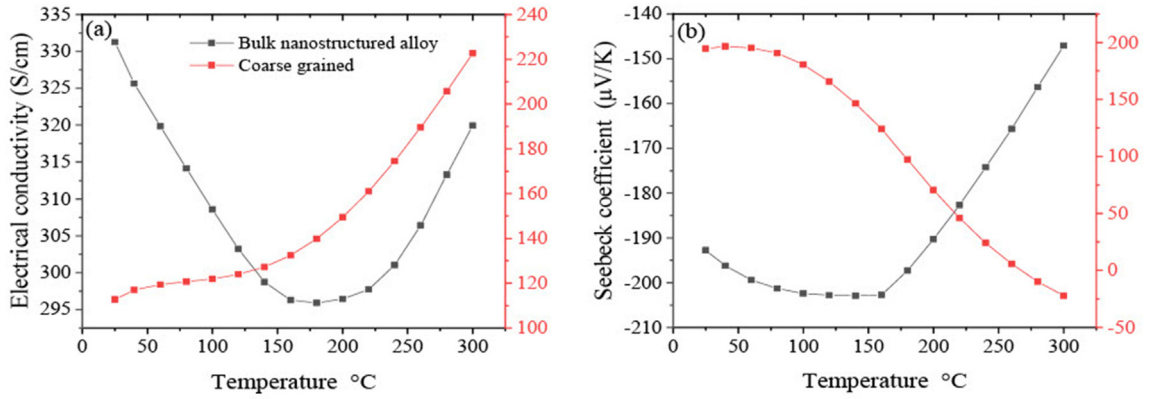

Fig. 8 – (a) Electrical conductivity and (b) Seebeck coefficient measurements for coarse-grained and bulk nanostructured $Bi_2Te_{2.55}Se_{0.45}$ samples.

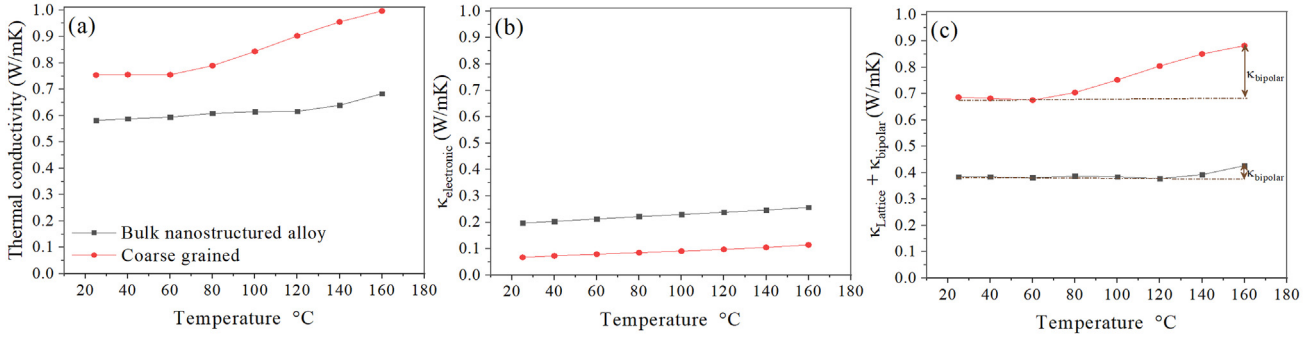

Fig. 9 – (a) Total thermal conductivity of the samples along with the (b) electronic, (c) lattice and bipolar thermal conductivity constituents.

and $\kappa_{bipolar}$ are observed due to the large grain size and low band gap, which in return increases the total thermal conductivity in the sample. Thus, the resulting microstructure and defect composition became less favorable for charge carrier transport properties.

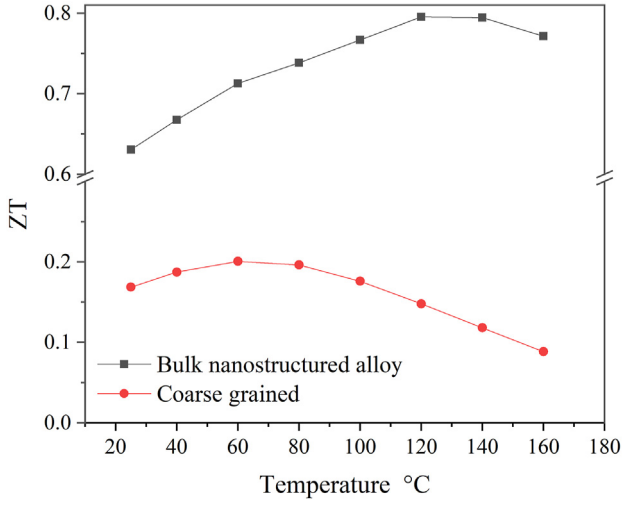

Fig. 10 – Figure-of-merit values for $Bi_2Te_{2.55}Se_{0.45}$ alloys prepared by different techniques.

Fig. 10 shows the thermoelectric figure-of-merit dependence on the preparation method of $Bi_2Te_{2.55}Se_{0.45}$ samples. A high ZT_{max} value of 0.80 at 120 °C was obtained for the bulk nanostructured sample, which is almost 400 % more than ZT_{max} of 0.20 at 60 °C obtained for the coarse-grained sample. This high ZT value of the bulk nanostructured $Bi_2Te_{2.55}Se_{0.45}$ sample is indeed an exceptional and competitive value when compared with reported ZT values for this composition in the literature. In 2016, Rimal et al. [49] prepared $Bi_2Te_{2.55}Se_{0.45}$ alloy by ball milling and spark plasma sintering techniques and reported a maximum ZT of 0.57 at 150 °C. Eum et al. [54] also prepared the same composition by ball milling and hot pressing. They reported a maximum ZT of 0.76 at 150 °C. It is worth mentioning that some studies have prepared similar Bi_2Te_3 systems in different forms, including films [59,71,72], and doped alloys [73], and reported a maximum ZT around 0.23 at 170 °C.

4. Conclusion

In the present investigation, we study the effect of the processing route on the microstructure and thermoelectric behavior of n-type $Bi_2Te_{2.55}Se_{0.45}$ alloy. Two processing techniques were adapted: ball milling/hot pressing (to

produce bulk nanostructured alloy) and induction melting/hot pressing/homogenization (to produce coarse-grained needle-like microstructured alloy). The obtained figure-of-merit values for the coarse needle-like structure and bulk nanostructured $Bi_2Te_{2.55}Se_{0.45}$ alloys are 0.20 and 0.80 at their optimum temperatures of 60 and 120 °C, respectively. Bulk nanostructured $Bi_2Te_{2.55}Se_{0.45}$ alloy outperformed the thermoelectric properties of coarse-grained alloy over the entire temperature range studied due to (i) higher electrical conductivity resulting from the donor-like effect induced by ball milling technique, (ii) more stable Seebeck coefficient (−200 to −140 μV/K) due to the larger band gap, and (iii) lower thermal conductivity caused by the lower adhesion and increased scattering at high grain boundaries. On the other hand, the induction melting route produced a unique, coarse needle-like microstructure with high lattice strain caused by intrinsic defects. This sample showed a p-type behavior as well as a charge carrier transition from p-to n-type (+200 to −25 μV/K) that is studied for the first time in $Bi_2Te_{2.55}Se_{0.45}$ alloys. Nevertheless, the large number of uncontrolled defects, small band gap, and the high bipolar effect caused noticeable deterioration in the thermoelectric properties of this sample. It is a given that no thermoelectric material can attain the best performance without introducing controlled defects. In fact, high thermal conductivity and unstable Seebeck coefficient are the primary reasons why the bipolar effect worsens the thermoelectric features. Hence, planning the appropriate defects through trying different $Bi_2(Te_{1-x}Se_x)_3$ compositions or adding a filler can promote the trade-off between carrier mobility and bipolar effect in the induction melting route.

Declaration of competing interest

The authors declare that they have no known competing financial interests or personal relationships that could have appeared to influence the work reported in this paper.

Acknowledgments

This work was supported by Grant no. GSRA8-L-1-0414-21013 and NPRP10−0206−170366 from Qatar National Research Fund (a member of the Qatar Foundation). The statements made herein are solely the responsibility of the authors. The authors acknowledge the technical support from the Central Laboratory Unit (CLU), the Center of Advanced Materials (CAM), and the Chemistry Department at Qatar University.

REFERENCES

[1] Ahmad K, Wan C, Al-Eshaikh MA, Kadachi AN. Enhanced thermoelectric performance of Bi_2Te_3 based graphene nanocomposites. Appl Surf Sci 2019;474:2−8.
[2] Jiang B, Wang W, Liu S, Wang Y, Wang C, Chen Y, et al. High figure-of-merit and power generation in high-entropy GeTe-based thermoelectrics. Science (New York, NY) 2022;377(6602):208−13.
[3] Gelbstein Y, Rosenberg Y, Sadia Y, Dariel MP. Thermoelectric properties evolution of spark plasma sintered (Ge0.6Pb0.3Sn0.1)Te following a spinodal decomposition. J Phys Chem C 2010;114(30):13126−31.
[4] Jeong H, Kihoi SK, Kim H, Lee HS. High seebeck coefficient and low thermal conductivity in Bi and in co-doped GeTe thermoelectric material. J Mater Res Technol 2021;15:6312−8.
[5] Liu H-T, Sun Q, Zhong Y, Deng Q, Gan L, Lv F-L, et al. High-performance in n-type PbTe-based thermoelectric materials achieved by synergistically dynamic doping and energy filtering. Nano Energy 2022;91:106706.
[6] Komisarchik G, Gelbstein Y, Fuks D. Solubility of Ti in thermoelectric PbTe compound. Intermetallics 2017;89:16−21.
[7] Schmitz A, Stiewe C, Zabrocki K, de Boor J, Mull K, Müller E. Current assisted sintering of PbTe—effects on thermoelectric and mechanical properties. Mater Res Bull 2017;86:159−66.
[8] Adam AM, Ibrahim EMM, Panbude A, Jayabal K, Veluswamy P, Diab AK. Thermoelectric power properties of Ge doped PbTe alloys. J Alloys Compd 2021;872:159630.
[9] Kaller M, Fuks D, Gelbstein Y. Sc solubility in p-type half-Heusler (Ti1-cScc)NiSn thermoelectric alloys. J Alloys Compd 2017;729:446−52.
[10] Huang L, Zhang Q, Yuan B, Lai X, Yan X, Ren Z. Recent progress in half-Heusler thermoelectric materials. Mater Res Bull 2016;76:107−12.
[11] Huang L, He R, Chen S, Zhang H, Dahal K, Zhou H, et al. A new n-type half-Heusler thermoelectric material NbCoSb. Mater Res Bull 2015;70:773−8.
[12] El-Khouly A, Adam AM, Altowairqi Y, Serhiienko I, Chernyshova E, Ivanova A, et al. Transport and thermoelectric properties of Nb-doped FeV0.64Hf0.16Ti0.2Sb half-Heusler alloys synthesized by two ball milling regimes. J Alloys Compd 2022;890:161838.
[13] El-Khouly A, Novitskii A, Serhiienko I, Kalugina A, Sedegov A, Karpenkov D, et al. Optimizing the thermoelectric performance of FeVSb half-Heusler compound via Hf-Ti double doping. J Power Sources 2020;477:228768.
[14] Guo D, Hu C, Zhang C. First-principles study on doping and temperature dependence of thermoelectric property of Bi2S3 thermoelectric material. Mater Res Bull 2013;48(5):1984−8.
[15] Thomas R, Rao A, Bhardwaj R, Wang L-Y, Kuo Y-K. Reduction in thermal conductivity and electrical resistivity in Cu2SnSe3/Cu2Se composite thermoelectric system. Mater Res Bull 2019;120:110607.
[16] Mangavati S, Rao A, Pal A, Kuo Y-K. The role of hetero-interface structures in enhancing the power factor of Cu2Se/x% Y2O3 composite thermoelectric materials. Mater Res Bull 2023;166:112362.
[17] Jin M, Bai X, Tang Z, Zhao S, Chen Y, Zhou L, et al. Fabrication of InSb crystal via Horizontal Bridgman method and investigation on its thermoelectric properties. Mater Res Bull 2021;142:111411.
[18] Lee SW, Kim T, Kim H-S, Park O, Kim DH, Kim S-i. Enhanced thermoelectric properties of InSe through simultaneous increase in electrical conductivity and Seebeck coefficient by Cl doping. J Mater Res Technol 2022;19:2077−83.
[19] Basha B, Jacob J, Tanveer Z, Ali A, Amin N, Javaid K, et al. Effect of source to the substrate distance on thermoelectric properties of copper nitride thin films grown by thermal evaporation method. J Mater Res Technol 2023;25:265−72.
[20] Jin M, Tang Z, Jiang J, Zhang R, Zhou L, Zhao S, et al. Growth of SnSe single crystal via vertical vapor deposition method and characterization of its thermoelectric performance. Mater Res Bull 2020;126:110819.

[21] Jin M, Jiang J, Li R, Wang X, Chen Y, Zhang R, et al. Growth of large size SnSe single crystal and comparison of its thermoelectric property with polycrystal. Mater Res Bull 2019;114:156–60.
[22] Kousar HS, Srivastava D, Karttunen AJ, Karppinen M, Tewari GC. p-type to n-type conductivity transition in thermoelectric CoSbS. Apl Mater 2022;10:091104.
[23] Li Y, Wang X, Liu G, Shin B, Shan F. High thermoelectric efficiency of p-type BiSbTe-based composites with CuGaTe2 nanoinclusions. Scripta Mater 2019;172:88–92.
[24] Elyamny S, Imam NG, Aquilanti G, Cabrera H, Kashyout AE-HB. Thermal transport properties for unveiling the mechanism of BiSbTe alloys in thermoelectric generation: a glance from synchrotron radiation Bi L3-XAFS. J Mater Res Technol 2022;18:2261–72.
[25] Lemine AS, El-Makaty FM, Al-Ghanim HA, Youssef KM. Experimental and modeling analysis of p-type Bi0.4Sb1.6Te3 and graphene nanocomposites. J Mater Res Technol 2022;16:1702–12.
[26] Kim BG, Seo KH, Lim C-H, Choi S-M. Different point defects originated from dissimilar deposition conditions in n-type Cu-doped Bi2Te3 films; crystal structure and thermoelectric property depending on Te-vacancy concentration. J Mater Res Technol 2021;15:606–13.
[27] Dou YC, Qin XY, Li D, Li YY, Xin HX, Zhang J, et al. Enhanced thermoelectric performance of BiSbTe-based composites incorporated with amorphous Si3N4 nanoparticles 2015;5:34251–6.
[28] Yamashita O, Ochi T, Odahara H. Effect of the cooling rate on the thermoelectric properties of p-type (Bi0.25Sb0.75)2Te3 and n-type Bi2(Te0.94Se0.06)3 after melting in the bismuth–telluride system. Mater Res Bull 2009;44(6):1352–9.
[29] Feutelais Y, Legendre B, Rodier N, Agafonov V. A study of the phases in the bismuth - tellurium system. Mater Res Bull 1993;28(6):591–6.
[30] Hu X, Fan Xa, Feng B, Kong D, Liu P, Xu C, et al. Evolution of microstructure and performance of n-type BiTeSe thermoelectric materials fabricated by multi-path equal channel angular extrusion. 2020. p. 24.
[31] Li AH, Shahbazi M, Zhou SH, Wang GX, Zhang C, Jood P, et al. Electronic structure and thermoelectric properties of Bi2Te3 crystals and graphene-doped Bi2Te3. Thin Solid Films 2010;518(Supplement):e57–60.
[32] An H, Pusko M, Chun D, Park S, Moon J. In-situ synthesis of flexible hybrid composite films for improved thermoelectric performance. Chem Eng J 2019;357:547–58.
[33] Zhang Q, Fang T, Liu F, Li A, Wu Y, Zhu T, et al. Tuning optimum temperature range of Bi2Te3-based thermoelectric materials by defect engineering. Chem Asian J 2020;15(18):2775–92.
[34] Madavali B, Lee C-H, Han J-G, Kim DH, Kim JT, Song G, et al. Investigation of homogeneity in microstructure and thermoelectric properties at various positions in high-thickness sintered bulks of p-type 20%Bi2Te3–80%Sb2Te3 alloys. J Mater Sci Mater Electron 2021;32(12):16302–10.
[35] Lou L-Y, Yang J, Zhu Y-K, Liang H, Zhang Y-X, Feng J, et al. Tunable electrical conductivity and simultaneously enhanced thermoelectric and mechanical properties in n-type Bi2Te3. Adv Sci 2022;9(27):2203250.
[36] Park D-H, Kim M-Y, Oh T-S. Thermoelectric energy-conversion characteristics of n-type Bi2(Te,Se)3 nanocomposites processed with carbon nanotube dispersion. Curr Appl Phys 2011;11(4):S41–5.
[37] Kim MY, Yeo YH, Park DH, Oh TS. Thermoelectric characteristics of the (Bi,Sb)2(Te,Se)3 nanocomposites processed with nanoparticle dispersion. Ceram Int 2012;38(Supplement 1):S529–33.
[38] Du B, Lai X, Liu Q, Liu H, Wu J, Liu J, et al. Spark plasma sintered bulk nanocomposites of Bi 2 Te 2.7 Se 0.3 nanoplates incorporated Ni nanoparticles with enhanced thermoelectric performance. ACS Appl Mater Interfaces 2019;11(35):31816–23.
[39] Kim C, Kim DH, Han YS, Chung JS, Park S, Park S, et al. Development of bismuth tellurium selenide nanoparticles for thermoelectric applications via a chemical synthetic process. Mater Res Bull 2011;46(3):407–12.
[40] Trawiński B, Bochentyn B, Gostkowska N, Łapiński M, Miruszewski T, Kusz B. Structure and thermoelectric properties of bismuth telluride—carbon composites. Mater Res Bull 2018;99:10–7.
[41] El-Makaty FM, Andre Mkhoyan K, Youssef KM. The effects of structural integrity of graphene on the thermoelectric properties of the n-type bismuth-telluride alloy. J Alloys Compd 2021;876:160198.
[42] Yang G, Sang L, Mitchell DRG, Fei Yun F, Wai See K, Jumlat Ahmed A, et al. Enhanced thermoelectric performance and mechanical strength of n-type BiTeSe materials produced via a composite strategy. Chem Eng J 2022;428:131205.
[43] Tae Kim K, Seong Eom Y, Son I. Fabrication process and thermoelectric properties of CNT/Bi2(Se,Te)3 composites. J Nanomater 2014;2015.
[44] Choi S-M, Lee KH, Lim YS, Seo W-S, Lee S. Effects of doping on the positional uniformity of the thermoelectric properties of n-type Bi2Te2.7Se0.3 polycrystalline bulks. J Kor Phys Soc 2016;68(1):17–21.
[45] Fuccillo MK, Jia S, Charles ME, Cava RJ. Thermoelectric properties of Bi2Te2Se compensated by native defects and Sn doping. J Electron Mater 2013;42(6):1246–53.
[46] Degen Ms T, Bron E, König U, Nénert G. The HighScore suite. Powder Diffr 2014;29(S 2):S 13–8.
[47] Riascos H, Duque JS, Orozco S, editors. Substrate temperature effects on the structure and properties of ZnMnO films prepared by pulsed laser deposition. Journal of Physics Conference Series; 2017 January 01; 2017.
[48] Sakalinien J, yvien J, Abakeviien B, Dudonis J. Investigation of structural and optical properties of GDC thin films deposited by reactive magnetron sputtering 2011;120(1):63–5.
[49] Rimal P, Han ST, Hong S-J, Kim H-S, Cho KY, Lee I. Effects of Bi2Se3 amount in thermoelectric performance of Bi2(TeSe)3 materials fabricated by high-energy ball milling. Int J Appl Ceram Technol 2016;13(4):711–7.
[50] El-Makaty FM, Ahmed HK, Youssef KM. Review: the effect of different nanofiller materials on the thermoelectric behavior of bismuth telluride. Mater Des 2021;209:109974.
[51] Zhu B, Yu Y, Wang X-y, Zu F-q, Huang Z-y. Enhanced thermoelectric properties of n-type BiTeSe semiconductor by manipulating its parent liquid state. J Mater Sci 2017;52(14):8526–37.
[52] El-Makaty FM, Ahmed HK, Youssef KM. Review: the effect of different nanofiller materials on the thermoelectric behavior of bismuth telluride. 2021. p. 209.
[53] Ma S, Li C, Wei P, Zhu W, Nie X, Sang X, et al. High-pressure synthesis and excellent thermoelectric performance of Ni/BiTeSe magnetic nanocomposites. J Mater Chem A 2020;8(9):4816–26.
[54] Eum A-Y, Kim I-h, Choi S-M, Lee S, Seo WS, Park J-S, et al. Thermoelectric and transport properties of mechanically-alloyed Bi2Te3-ySey solid solutions. J Kor Phys Soc 2015;67:1809–13.
[55] Eum AY, Choi S-M, Lee S, Seo W-S, Park J-S, Yang S-H, et al. Thermoelectric properties of Bi2Te3–ySey:ImPrepared by mechanical alloying and hot pressing. J Electron Mater 2017;46(5):2623–8.

[56] Oh TS, Hyun D-B, Kolomoets NV. Thermoelectric properties of the hot-pressed (Bi,Sb)2(Te,Se)3 alloys. Scripta Mater 2000;42(9):849–54.
[57] Horák J, Stary Z, Lošťák P, Pancíř J. Anti-site defects in n-Bi2Se3 crystals. J Phys Chem Solid 1990;51(12):1353–60.
[58] Ibrahim EMM, Mohamed MAA, Ali HM, Khavrus VO, Hampel S, Wakkad MM. Optical and transport properties of few quintuple-layers of Bi2-xSbxSe3 nanoflakes synthesized by hydrothermal method. J Alloys Compd 2019;804:272–80.
[59] Adam AM, Ibrahim EMM, Panina LV, Petkov P. Optical and thermoelectric properties of nanocrystalline Bi2(Se1-xTex)3 films. Nanoscale Microscale Thermophys Eng 2018;22(1):21–38.
[60] Shokr EK, Ibrahim EMM, Abdel Hakeem AM, Adam AM. Structural, electrical, and thermoelectrical properties of (Bi1-xSbx)2Se3 alloys prepared by a conventional melting technique. Soviet Journal of Experimental Theoretical Physics 2013;116:166–72.
[61] Adam AM, Elshafaie A, Mohamed AE-MA, Petkov P, Ibrahim EMM. Thermoelectric properties of Te doped bulk Bi2Se3 system. Mater Res Express 2018;5(3):035514.
[62] Adam AM, Diab AK, El-Hadek MA, Sayed AO, Ibrahim EMM. Electrical and thermoelectrical properties of Bi2−xNaxTe3 alloys. J Alloys Compd 2022;920:165952.
[63] Hong M, Chen Z-G, Zou J. Fundamental and progress of Bi2Te3-based thermoelectric materials. Chin Phys B 2018;27(4):048403.
[64] Chasmar RP, Stratton R. The thermoelectric figure of merit and its relation to thermoelectric generators. Journal of Electronics Control 1959;7(1):52–72.
[65] Mahan GD. Figure of merit for thermoelectrics. J Appl Phys 1989;65(4):1578–83.
[66] Sofo JO, Mahan GD. Optimum band gap of a thermoelectric material. Phys Rev B 1994;49(7):4565–70.
[67] Mehdizadeh Dehkordi A, Zebarjadi M, He J, Tritt TM. Thermoelectric power factor: enhancement mechanisms and strategies for higher performance thermoelectric materials. Mater Sci Eng R Rep 2015;97:1–22.
[68] Greenaway DL, Harbeke G. Band structure of bismuth telluride, bismuth selenide and their respective alloys. J Phys Chem Solid 1965;26(10):1585–604.
[69] Zhang Y, Ma H, Sun B, Liu B, Liu H, Kong L, et al. Thermoelectric performance of graphene composited BiSbTe bulks by high pressure synthesis. J Alloys Compd 2017;715:344–8.
[70] Kim D-H, Mitani T. Thermoelectric properties of fine-grained Bi2Te3 alloys. J Alloys Compd 2005;399(1):14–9.
[71] Adam AM, Elsehly EM, Ataalla M, El-Khouly A, Nafady A, Diab AK. Preparation and thermoelectric power properties of highly doped p-type Sb2Te3 thin films. Phys E Low-dimens Syst Nanostruct 2021;127:114505.
[72] Adam AM. Characterization of thin Bi2Te3-based films and effects of heat treatment on their optical properties. J Alloys Compd 2018;765:1072–81.
[73] Adam AM, El-Khouly A, Diab AK. Effects of transition metal element doping on the structural and thermoelectric properties of n-type Bi2-xAgxSe3 alloys. J Alloys Compd 2021;851:156887.